

# Hierarchical Porous Metal–Organic Polyhedra for Efficient Oxidative Cleavage of $\beta$ -O-4 Bonds in Lignin Model Compound

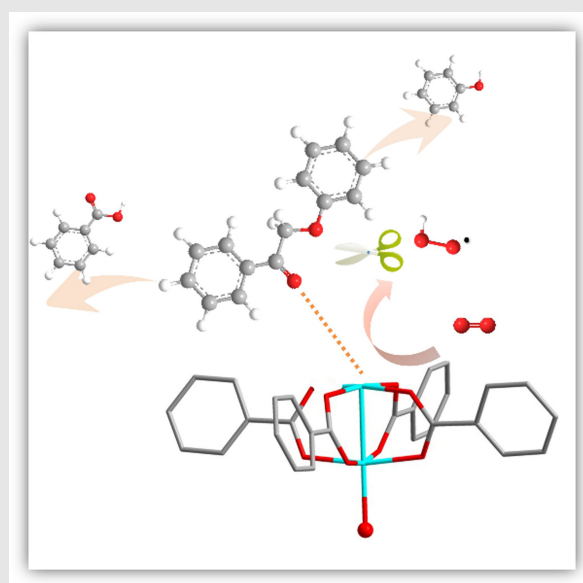
Xinchen Kang<sup>1,2</sup>, Lili Li<sup>1</sup>, Hengan Wang<sup>2</sup>, Tian Luo<sup>1</sup>, Shaojun Xu<sup>3,4,5</sup>, Yinlin Chen<sup>1</sup>, Joseph H. Carter<sup>1,6</sup>, Zi Wang<sup>1</sup>, Alena M. Sheveleva<sup>1</sup>, Kai Lyu<sup>1</sup>, Xue Han<sup>1,7</sup>, Floriana Tuna<sup>1,8</sup>, Eric J. L. McInnes<sup>1,8</sup>, Chiu C. Tang<sup>6</sup>, Lifei Liu<sup>2</sup>, Buxing Han<sup>2</sup>, Emma K. Gibson<sup>4,9</sup>, C. Richard A. Catlow<sup>3,4,10</sup>, Sihai Yang<sup>1,11\*</sup> & Martin Schröder<sup>1\*</sup>

<sup>1</sup>Department of Chemistry, The University of Manchester, Manchester M13 9PL, <sup>2</sup>Beijing National Laboratory for Molecular Sciences, CAS Key Laboratory of Colloid, Interface and Chemical Thermodynamics, Institute of Chemistry, Chinese Academy of Science, Beijing 100190, <sup>3</sup>School of Chemistry, Cardiff University, Cardiff CF10 3AT, <sup>4</sup>UK Catalysis Hub, Research Complex at Harwell, Rutherford Appleton Laboratory, Harwell OX11 0FA, <sup>5</sup>Department of Chemical Engineering, The University of Manchester, Manchester M13 9PL, <sup>6</sup>Diamond Light Source, Harwell Science Campus, Oxfordshire OX11 0DE, <sup>7</sup>College of Chemistry, Beijing Normal University, Beijing 100875, <sup>8</sup>Photon Science Institute, The University of Manchester, Manchester M13 9PL, <sup>9</sup>School of Chemistry, Joseph Black Building, University of Glasgow, Glasgow G12 8QQ, <sup>10</sup>Department of Chemistry, University College London, London WC1H 0AJ, <sup>11</sup>Beijing National Laboratory for Molecular Sciences, College of Chemistry and Molecular Engineering, Peking University, Beijing 100871

\*Corresponding authors: [sihai.yang@manchester.ac.uk](mailto:sihai.yang@manchester.ac.uk); [m.schroder@manchester.ac.uk](mailto:m.schroder@manchester.ac.uk)

**Cite this:** *CCS Chem.* **2025**, Just Published. DOI: 10.31635/ccschem.024.202404991

Catalytic cleavage of  $\beta$ -O-4 linkages is an essential but challenging step in the depolymerization of lignin. Here, we report the templated electrosynthesis of a hydrophobic metal-organic polyhedral catalyst (Cu-MOP-e), which exhibits excellent hydrothermal stability and exceptional activity for this reaction. The oxidative cleavage of 2-phenoxyacetophenone, **1**, a lignin model compound, over Cu-MOP-e at 90 °C for 1 h affords full conversion with yields of the monomer products phenol and benzoic acid of 99%. The reusability of Cu-MOP-e was confirmed by carrying out ten cycles of reaction. The mechanism of catalyst-substrate binding was investigated by high-resolution synchrotron X-ray powder diffraction, in situ X-ray absorption spectroscopy, electron paramagnetic resonance spectroscopy, and density functional theory (DFT) calculations. The combination of optimal porosity and active Cu(II) sites provides confined binding of 2-phenoxyacetophenone, thus promoting the cleavage of  $\beta$ -O-4 linkage under relatively mild conditions.



**Keywords:** metal–organic polyhedra, porous structure, defects, host-guest interactions, cleavage of  $\beta$ -O-4 linkages

## Introduction

The utilization of porous metal-organic complexes as heterogeneous catalysts has attracted much interest owing to their inherent flexibility to tailor their active sites within a microenvironment.<sup>1-4</sup> In addition to functional ligands that can act as active sites in catalysis, the generation of open metal sites via the removal of labile metal-bound solvent molecules enables these porous solids to act as Lewis acids<sup>5,6</sup> that can interact with substrate molecules.<sup>7,8</sup> Porous metal-organic solids that possess pore sizes at the subnanometer scale often demonstrate limited diffusion of substrates, especially with large molecules, in heterogeneous reactions in solution.<sup>9,10</sup> Inaccessible channels result in poor usage of active sites and low catalytic efficiency.<sup>11,12</sup> Metal-organic polyhedra (MOPs), comprised of discrete metal-organic molecular assemblies stabilized by van der Waals interaction, can show significant porosity, and thus, parallel related framework-based materials.<sup>13</sup> Porosity in MOPs originates primarily from the void within the polyhedral cage, but also from potential large voids generated by packing of cages in three-dimensional space.<sup>14,15</sup> The latter can greatly facilitate the adsorption of large substrates and promote internal diffusion throughout the solid-state structure. In addition, the engineering of defects within the material is an effective way to generate active metal sites and build channels to enable diffusion of reactants and products.<sup>16,17</sup>

Porous {Cu<sub>2</sub>}-paddlewheel-based metal-organic frameworks (MOFs) and MOPs with open Cu(II) sites have been reported as efficient catalysts for a series of reactions.<sup>18,19</sup> However, the lack of hydrolytic stability is a disadvantage for their application in heterogeneous catalysis.<sup>20</sup> Herein, we report a hydrophobic Cu-carboxylate MOP material with a hierarchically porous structure (denoted as Cu-MOP-e; e signifies electrosynthesis), prepared via templated electrosynthesis in an ionic liquid (IL)-containing electrolyte. Cu-MOP-e exhibits exceptional activity and stability for the oxidative cleavage of β-O-4 linkage in the lignin model compound, 2-phenoxyacetophenone **1**, and shows quantitative conversion into monomer products of phenol and benzoic acid in water at 90 °C within 1 h. Compared with Cu-MOP-t (t signifies thermal synthesis) and several benchmark Cu-MOFs obtained using conventional solvothermal methods, the use of assemblies of ILs as templates in the electrosynthesis not only increases the number of mesopores in Cu-MOP-e to enhance the accessibility of **1** to active Cu(II) sites via accelerated diffusion but also increases the number of uncoordinated Cu(II) sites to promote the activation of **1** and O<sub>2</sub>. The underlying catalytic mechanism was interrogated by in situ high-resolution synchrotron X-ray powder diffraction (SXPDP), in situ small angle X-ray scattering (SAXS), in situ X-ray

absorption fine structure (XAFS) spectroscopy analysis, electron paramagnetic resonance (EPR) spectroscopy and density functional theory (DFT) calculations. These studies have provided insights into the design of new stable MOP-based catalysts, incorporating hierarchical porosity and defects for biomass conversion.

## Experimental Methods

### Solvothermal synthesis of Cu-MOP-t and other Cu-MOFs

Cu(NO<sub>3</sub>)<sub>2</sub> · 3H<sub>2</sub>O (0.484 g, 2 mmol) and ligand (0.133 g, 0.2 mmol) were separately dissolved in small portions of dimethylformamide (DMF) before being combined in a round bottom flask and diluted to a total volume of 50 mL.<sup>21</sup> The mixture was stirred at 85 °C for 24 h under reflux. The precipitate was collected and washed with DMF and acetone, five times each, and dried at 60 °C for 24 h. The yield of Cu-MOP-t was 49%.

### Templated electrosynthesis of Cu-MOP-e

The synthesis was performed in a 50 mL single cell using a two-electrode system with a CHI660E electrochemical workstation (CH Instruments, Inc., Austin, Texas, USA). Cu-foam (2.0 × 1.0 cm<sup>2</sup>) was used as both cathode and anode with a solution of 50 mL OmimPF<sub>6</sub>/DMF (w/w = 4/1) as electrolyte. The ligand (0.133 g, 0.2 mmol) was dissolved in the electrolytic solution and a potential of 2 V at 25 °C was applied. A blue precipitate formed after several minutes and the electrolysis was continued for a further 12 h. After the reaction, the precipitate was collected and washed with DMF and acetone, each five times, and the solid dried at 60 °C for 24 h. The yield of Cu-MOP-e was 95%.

### Oxidative cleavage of **1**

All oxidation reactions were carried out in a three-necked flask using the same protocol. **1** (0.1 mmol) and catalyst [0.04 mmol, based on the Cu content determined by inductively coupled plasma optical emission spectroscopy (ICP-OES)] were loaded into 2 mL of DMF. The air in the flask was replaced by O<sub>2</sub>, and the flask was immersed in an oil bath at the desired temperature. O<sub>2</sub> was supplied by a balloon. After the reaction, the catalyst was collected and the solution at the targeted reaction time was analyzed by gas chromatography. To collect used Cu-MOP-e, the reaction mixture was centrifuged at a speed of 16,000 r/min and the solid collected, washed with acetone, dried at 60 °C for 24 h, and reused for the next run. The rate constants of reaction at different temperatures were calculated based upon the variation of concentration of reactant during the reaction, and the

activation energy was calculated depending on rate constants at different temperatures.

More experimental details and characterization are available in the [Supporting Information](#).

## Results and Discussion

### Synthesis, structural analysis, and characterization of Cu-MOPs

Cu-MOP derived from the hydrophobic ligand, H<sub>3</sub>L, was selected for investigation for the cleavage of β-O-4 linkages in **1** owing to its high stability and large channels that can promote internal diffusion ([Supporting Information Figures S1 and S2](#)).<sup>21,22</sup> The crystal structure of Cu-MOP exhibits a small cavity within a [Cu<sub>12</sub>L<sub>8</sub>] cage and two types of intermolecular cavities originating from the packing of these cages. Cu-MOP-t was obtained from a solvothermal reaction following our previously reported methods.<sup>21,22</sup> Cu-MOP-e was synthesized electrochemically at 2.0 V and 25 °C in an IL-rich electrolyte containing 80 wt % 1-octyl-3-methylimidazolium hexafluorophosphate (OmimPF<sub>6</sub>, [Supporting Information Figure S3](#)) and 20 wt % DMF using Cu foams as both cathode and anode. The electrolyte turned turbid within several minutes and the reaction was terminated on depletion of ligand in the electrolyte to give a yield of Cu-MOP-e of ~97%. The contact angles between the MOP and water interface were recorded as 90.6° and 89.7° for Cu-MOP-t

and Cu-MOP-e ([Supporting Information Figure S4](#)), respectively, reflecting the hydrophobicity of both materials. The phase identity of Cu-MOP-t and Cu-MOP-e was confirmed by powder X-ray diffraction (PXRD, [Figure 1a](#)), and the shape of the convoluted peaks observed for Cu-MOP-e implied a defective structure. Compared with Cu-MOP-t, the ν(C=O) stretching mode of the carboxylate group in Cu-MOP-e showed a blueshift from 1403 to 1407 cm<sup>-1</sup> in the Fourier transform infrared (FTIR) spectra, consistent with increased levels of free carboxylic groups in the latter ([Figure 1b](#)).<sup>23</sup> Free IL was not observed in the Cu-MOP-e by FTIR spectroscopy ([Figure 1b](#)). Transmission electron microscopy (TEM) confirmed the well-defined polyhedral morphology of Cu-MOP-t with a particle size of ~2.5 μm ([Figure 1c](#)). In contrast, Cu-MOP-e exhibited irregular morphology with substantial mesopores of ~4 nm ([Figure 1d](#)), originating from the high viscosity of self-assemblies of the ILs that mediate nucleation during crystal growth.<sup>24</sup> N<sub>2</sub> adsorption/desorption isotherms of Cu-MOP-t and Cu-MOP-e at 77 K showed intermediate profiles between Type I and IV ([Supporting Information Figure S5](#)), suggesting the presence of both micropores and mesopores. Cu-MOP-e exhibited a slightly lower total surface area than Cu-MOP-t (675 and 746 m<sup>2</sup> g<sup>-1</sup>, respectively; [Supporting Information Table S1](#)). Analysis of the pore size distribution by the Horvath-Kawazoe method<sup>25</sup> ([Figure 1e](#)) revealed a narrow peak centered at ~6 Å, assigned to the cavities within the cage. The existence of mesopores

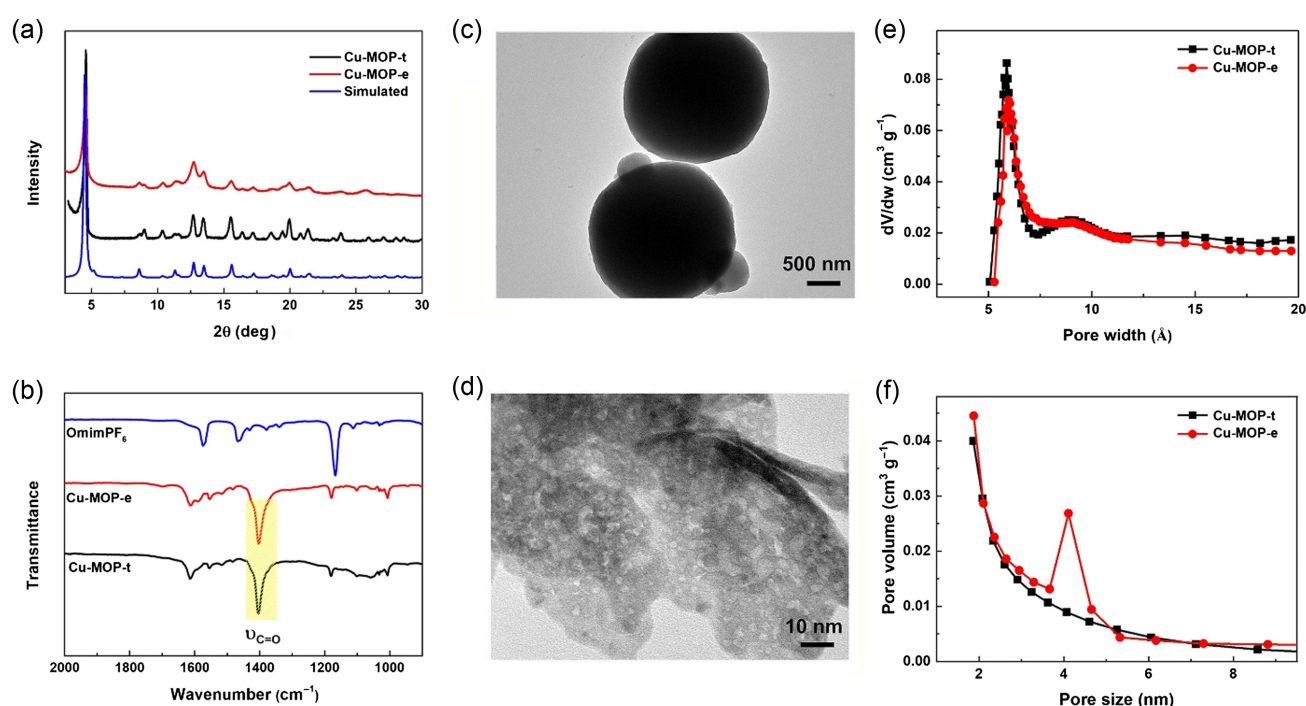


**Figure 1** | Structure and morphology of Cu-MOPs. (a) PXRD patterns. (b) FTIR spectra. (c) TEM image of Cu-MOP-t. (d) TEM image of Cu-MOP-e. (e) Micropore size distribution. (f) Mesopore size distributions.

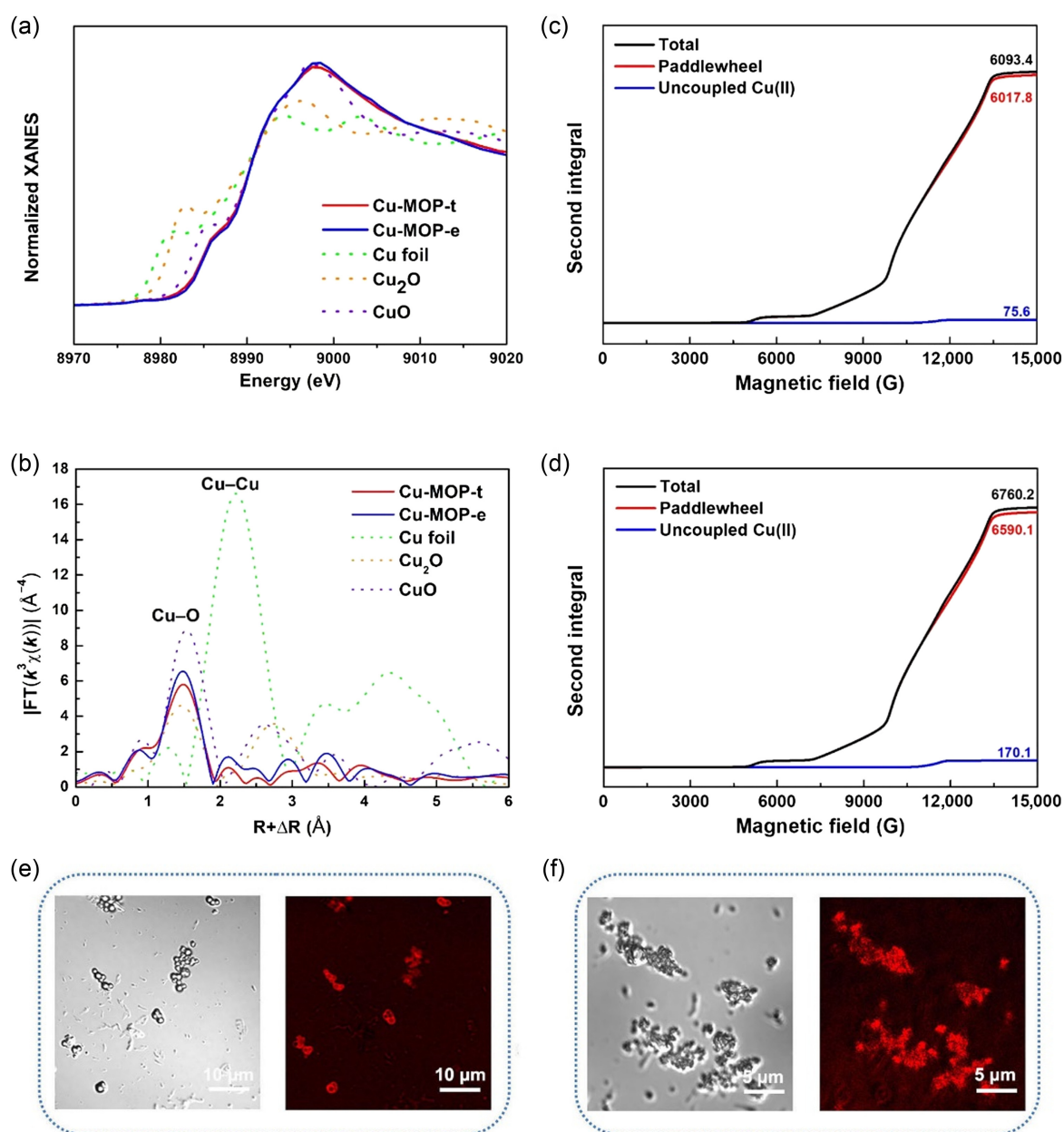


**Figure 2** | Morphology and porosity of Cu-MOP. (a) Normalized Cu K-edge XANES spectra. (b) The Cu K-edge FT-EXAFS spectra without phase correction. (c, d) Second integrals of simulated Q-band EPR spectra for Cu-MOP-t (c) and Cu-MOP-e (d). (e, f) Comparison of the microphotographs (left) and CFM images (right) of Cu-MOP-t (e) and Cu-MOP-e (f).

in Cu-MOPs with a distribution from 2 to 6 nm was confirmed by the Barrett-Joyner-Halenda analysis (Figure 1f). The nature of pores derived from  $N_2$  isotherms was consistent with the findings derived from structural data,<sup>22</sup> and a major contribution of mesopores of 4.0 nm was observed for Cu-MOP-e consistent with TEM measurements.

Cu-MOP-e is less crystalline than Cu-MOP-t (Figure 1a), suggesting that the former incorporates substantial crystal defects. The X-ray absorption near-edge structure (XANES) revealed that both Cu-MOP-t and Cu-MOP-e

were aligned with that of CuO, confirming the Cu(II) valence (Figure 2a and Supporting Information Figure S6). The Fourier-transformed extended X-ray absorption fine structure (FT-EXAFS) spectra confirmed Cu-O scattering paths for all catalysts, similar to CuO (Figure 2b). The coordination number (CN) of Cu-O was determined through quantitative fitting of the FT-EXAFS curves (Supporting Information Table S2 and Figures S7-S10), with values of 4.85 and 4.57 for Cu-MOP-t and Cu-MOP-e, respectively. This indicated that the defect structure in the Cu-MOP-e might derive from the cleavage of Cu-O

interactions. Cu-MOP-t and Cu-MOP-e contained 0.52% and 1.08% of uncoupled Cu(II) sites, respectively, based on the relative intensity of the second integral of simulations of the Q-band EPR spectra (Figure 2c,d; Supporting Information Figures S11–S12 and Tables S3–S4).<sup>26</sup> Thus, cleavage of Cu–O bonds leads to increased numbers of uncoordinated Cu(II) sites, with a concomitant increase in the Lewis acidity of Cu-MOP-e. The presence of Lewis acid sites within these Cu-MOP materials was revealed unambiguously by confocal fluorescence microscopy (CFM) (Figure 2e,f), which exhibited strong fluorescence originating from the open Cu(II) sites, as detected via a reaction with furfuryl alcohol used as a probe.<sup>27</sup> The observed fluorescence confirmed the presence of open Cu(II) sites derived from the removal of water bound to Cu(II) and/or due to the presence of Cu(II) defects. Fluorescence was observed only at particle boundaries in Cu-MOP-t but throughout the entire lattice of Cu-MOP-e, confirming the presence of an increased number of open Cu(II) sites throughout Cu-MOP-e. During the synthesis of Cu-MOP-e, IL plays a significant role in controlling its structure and morphology. The strong electrostatic interactions between IL cations and ligand

anions affect the coordination of Cu<sup>2+</sup> with L<sup>3-</sup>, leading to a reduced coordination number at Cu(II). Additionally, aggregates of IL cations could act as a template for mesopore formation.<sup>25</sup> As a result, Cu-MOP-e synthesized in an IL-based solution incorporated both open Cu(II) sites and mesopores, which enhance reactant activation and facilitate mass transfer during catalytic reactions.

## Studies of catalytic activity

Lignin is an abundant renewable aromatic resource and can be upgraded to a wide range of aromatic feedstocks via lignin depolymerization.<sup>28–30</sup> The β-O-4 linkage accounts for approximately 50% of the interunit linkages in lignin, and catalytic conversion of various model compounds of lignin-containing this substructure including cracking, hydrolysis, reductive and oxidative methods have been studied.<sup>31–35</sup> Transition metals are efficient catalysts for the oxidative depolymerization of the β-O-4 linkage in protic solvents.<sup>36,37</sup> Thus, we sought to test the performance of the above Cu-MOPs for the oxidative cleavage of β-O-4 linkage in **1** to produce

**Table 1** | Comparisons of Different Catalysts for the Oxidative Cleavage of **1**

Reaction scheme: O=C(O)c1ccc(OCC2=CC=CC=C2)cc1 + O2 -> Oc1ccccc1 + O=C(O)c1ccccc1

Entry	Catalysts	T (°C)	t (h)	Conv. (%)	Yield (%)		Ref
					Phenol	Benzoic Acid	
1 <sup>a</sup>	Cu-MOP-t	90	1	59.7	59.5	58.9	This work
2 <sup>a</sup>	Cu-MOP-e	90	1	>99	>99	>99	This work
3 <sup>a</sup>	MFM-100	90	1	14.4	14.2	14.1	This work
4 <sup>a</sup>	HKUST-1	90	1	8.4	8.2	8.2	This work
5 <sup>a</sup>	MOF-2	90	1	11.2	11.0	10.8	This work
6 <sup>a</sup>	—	90	1	2.8	2.6	2.5	This work
7 <sup>a</sup>	OmimPF <sub>6</sub>	90	1	3.2	3.0	2.7	This work
8 <sup>a</sup>	Cu(Ac) <sub>2</sub>	90	1	11.7	11.2	11.2	This work
9 <sup>a</sup>	MFM-100-e	90	1	35.2	34.9	34.8	This work
10 <sup>b</sup>	CeO <sub>2</sub>	160	2	76	58	2.8	<sup>39</sup>
11 <sup>b</sup>	Au/CeO <sub>2</sub>	160	2	>99	71.1	12.3	<sup>39</sup>
12 <sup>c</sup>	Cu(Ac) <sub>2</sub> +Phen	90	2	97	96	70	<sup>40</sup>
13 <sup>d</sup>	BnmimNTf <sub>2</sub>	130	3	>99	84	89	<sup>35</sup>
14 <sup>e</sup>	OmimAc	100	2	>99	96	86	<sup>31</sup>

<sup>a</sup> Reaction conditions: 0.1 mmol of **1**, 0.04 mmol of catalyst, 2 mL of DMF/water (3:1), 1 atm O<sub>2</sub>.

<sup>b</sup> Reaction conditions: 0.47 mmol of **1**, 20 mg catalyst, 25 mL of CH<sub>3</sub>OH, 1.0 MPa O<sub>2</sub>. The Au content in entry **11** is 0.88 wt %.

<sup>c</sup> Reaction conditions: 0.2 mmol of **1**, 0.04 mmol of catalyst, 0.4 mmol of acid, 2 mL of CH<sub>3</sub>OH, 0.4 MPa O<sub>2</sub>, homogeneous catalysis. Phen represents 1,10-phenanthroline (0.04 mmol, entry **12**).

<sup>d</sup> Reaction conditions: 1 mmol of **1**, 1 g of catalyst, 16 μL of H<sub>3</sub>PO<sub>4</sub> (85%), 46 μL of H<sub>2</sub>O, 1.0 MPa O<sub>2</sub>, homogeneous catalysis.

<sup>e</sup> Reaction conditions: 1 mmol of **1**, 1 g of catalyst, 25 μL of H<sub>2</sub>O, 1.5 of MPa O<sub>2</sub>, homogeneous catalysis.

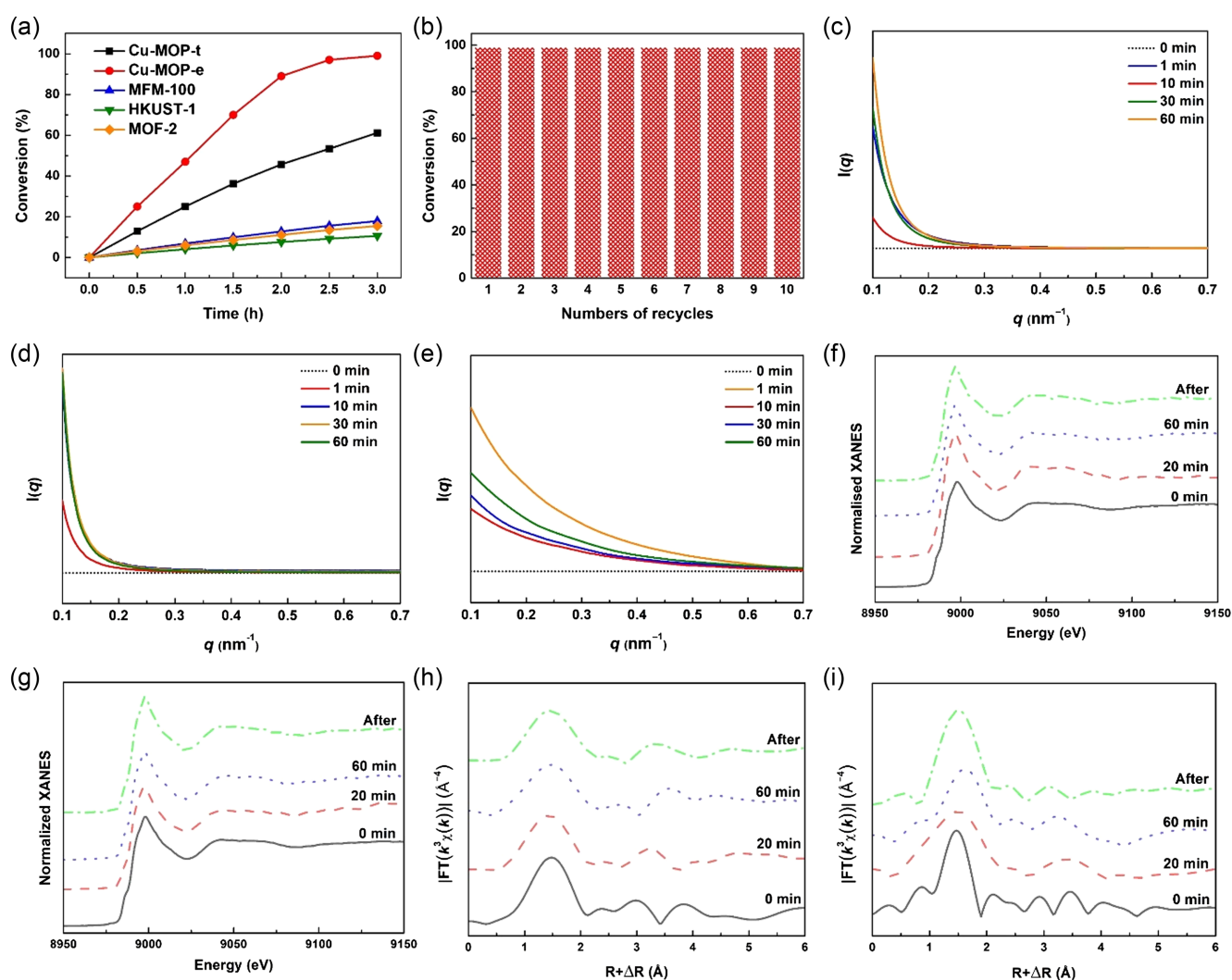


**Figure 3** | Catalytic performance of different Cu(II)-paddlewheel-based catalysts. (a) Plot of conversion vs time for different catalysts. (b) Reusability of Cu-MOP-e. (c–e) In situ SAXS of diffusion of **1** within Cu-MOP-t (c), Cu-MOP-e (d) and HUKST-1 (e). (f, g) In situ Cu K-edge XANES spectra over Cu-MOP-t (f) and Cu-MOP-e (g) during the cleavage of **1**. (h, i) In situ Cu K-edge FT-EXAFS spectra over Cu-MOP-t (h) and Cu-MOP-e (i) during the cleavage of **1**. Reaction conditions: 0.1 mmol **1**, 0.04 mmol catalyst, 2 mL DMF/water (3:1), 80 °C, 1 atm O<sub>2</sub>.

phenol and benzoic acid. Water was used both as a solvent and proton source for this reaction, and its relatively high boiling point can drive the reaction under ambient pressure. The selected benchmark {Cu<sub>2</sub>}-paddlewheel-based MOFs, mesoporous Cu(II)-MOF (MFM-100), HKUST-1, and MOF-2 have also been prepared by solvothermal synthesis (Supporting Information Figures S13–S14 and Table S1) and tested for this reaction to afford a direct comparison between these MOF- and MOP-based catalysts.

Phenol and benzoic acid were the only products detected in this study, indicating that the paddlewheel structure with Cu(II) sites was highly selective for the cleavage of β-O-4 bonds. Cu-MOP-t and Cu-MOP-e exhibited conversions of **1** of 59.7% and >99%, respectively, at 90 °C and 1 h under 1 atm of O<sub>2</sub>. The conversions

are higher than that with MFM-100 (14.4%), HKUST-1 (8.4%), and MOF-2 (11.2%) under the same conditions (Table 1). The turnover frequency (TOF) observed for Cu-MOP-e was 60% higher than that of Cu-MOP-t (Supporting Information Table S5), and the former displayed rapid conversion of **1**, as confirmed by the studies of conversion versus time at 80 °C (Figure 3a). Conversion increased to ~90% over the first 2 h and then slowed down until full conversion was reached at 3 h. The concentration of **1** over Cu-MOP-e decreased linearly with reaction time, as it did with other catalysts studied here (Supporting Information Figure S15), indicative of a first-order kinetic reaction. The rate constant and activation energy for this reaction over these catalysts were derived from the reaction data and application of the Arrhenius equation (Supporting Information Table S6 and Figure

S16).<sup>38</sup> The Cu-MOPs exerted lower activation energies than {Cu<sub>2</sub>}-paddlewheel-based MOFs, with Cu-MOP-e showing the lowest activation energy (Supporting Information Figure S16).

A leaching test was conducted by removing Cu-MOP-e via hot filtration of the reaction solution at ~50% conversion, after which little further conversion was observed, indicating the absence of leaching of the catalytically-active Cu(II) species into the reaction system (Supporting Information Figure S17). Cu-MOP-e also showed excellent stability over 10 cycles of reaction with little loss of activity (Figure 3b). Retention of crystal structure and morphology of the used Cu-MOP-e catalyst after repeated cycles were also confirmed (Supporting Information Figures S18 and S19). Little conversion of **1** was observed in the absence of a catalyst or using the IL OmimPF<sub>6</sub> as the catalyst, confirming that Cu(II) sites were required for the reaction to proceed (Table 1). Copper acetate gave an 11.7% conversion of **1** at 90 °C after 1 h, similar to the performance of tested MOF-based catalysts (Table 1). MFM-100 catalyst was also prepared by templated electrosynthesis to give a material denoted as MFM-100-e. Analysis of the structure and porosity confirmed that MFM-100-e showed reduced crystallinity and the presence of mesopores (Supporting Information Figures S20–S21 and Table S1). MFM-100-e gave a significantly higher TOF value than MFM-100-t at 90 °C (Table 1), confirming that templated electrosynthesis played a key role in boosting catalytic activity. However, MFM-100-e showed a lower conversion of **1** than the Cu-MOPs. A comparison of the catalytic performance for the cleavage of **1** by Cu-MOPs and state-of-the-art catalysts in the literature is summarized in Table 1,<sup>31,35,39,40</sup> which suggests that Cu-MOP-e exhibited the best performance.

## Mechanistic study

MFM-100, HKUST-1, and MOF-2 showed similar performance but notably reduced catalytic activity compared with Cu-MOP-t and Cu-MOP-e (Table 1). The shared {Cu<sub>2</sub>}-paddlewheel structure between Cu-MOP and these MOFs suggests that this structural feature alone is not the primary determinant of their reaction activity, but rather, likely due to differences in their pore sizes, with Cu-MOP incorporating much larger pores compared with these MOFs. The mesopores in Cu-MOP enhance both the adsorption of **1** and mass transfer during the reaction, contributing to the superior performance of Cu-MOP-t and Cu-MOP-e. We conducted in situ SAXS to investigate the dispersion kinetics of **1** within Cu-MOP-t, Cu-MOP-e, and HKUST-1 (Figure 3c–e). In the absence of **1**, the system which contained catalyst and solvent only was measured as the background. Upon addition of **1** and subtracting the background, the SAXS signal reflected an aggregation of **1** within the pores of the catalysts. According to Guinier's Law, a steeper SAXS

slope indicates larger aggregate sizes, with the rate of increase of aggregate size dependent on the diffusion rate of **1** from the solvent into the catalyst pores. From the in situ SAXS curves, the diffusion of **1** in Cu-MOP-t and Cu-MOP-e reached equilibrium within 10 min. Conversely, the SAXS slope for HKUST-1 steepened progressively over time, suggesting a gradual dispersion of **1** into the pores of HKUST-1. Furthermore, Cu-MOP-t and Cu-MOP-e exhibited significantly steeper SAXS slopes compared with HKUST-1, indicating a notably higher diffusion kinetics of **1** within Cu-MOP-t and Cu-MOP-e than within HKUST-1. Cu-MOP-e demonstrated slightly enhanced diffusion kinetics compared with Cu-MOP-t, reflecting increased mesoporous structure in the former.

While Cu-MOP-t and Cu-MOP-e displayed similar diffusion kinetics for **1**, their catalytic performances differed significantly. To investigate this observation, in situ X-ray absorption spectroscopy (XAS) was utilized to analyze the variance in chemical states and local fine structure of Cu-MOP-t and Cu-MOP-e throughout the reaction process (Figure 3f–i). The in situ XANES spectra confirmed that neither Cu-MOP-t nor Cu-MOP-e underwent valence state changes during the reaction (Figure 3f,g). While Cu-MOP-t exhibited minimal variation in the Cu–O bond length over time, the Cu–O bond in Cu-MOP-e gradually lengthened during the reaction but returned to its original state after complete removal of the reactants, as indicated by in situ FT-EXAFS spectra (Figure 3h,i). The extended Cu–O bond of Cu-MOP-e during the reaction suggests that Cu-MOP-e interacted significantly with the reactants owing to the presence of uncoordinated Cu(II) sites.

The direct interaction between Cu-MOP and **1** was studied to understand the excellent catalytic performance. Cu-MOP-t was selected owing to its high crystallinity and the preferred binding domain of **1** within Cu-MOP-t was determined by Rietveld refinement of the SXP data (Figure 4a–c and Supporting Information Figure S22).<sup>41</sup> **1** was found within the cavity of the MOP cage with an occupancy of one molecule per cage, with the carbonyl oxygen of **1** replacing the coordinated water molecule and binding to the Cu(II) sites (Cu···O = 2.238 Å). Due to steric effects, the torsion angle in **1** between two benzene rings change from 13.8° to 47.4° on binding within Cu-MOP-t (Figure 4c).<sup>42</sup> Adsorption of **1** into Cu-MOP was also confirmed by FTIR spectroscopy (Supporting Information Figure S23). Cu-MOP-e exhibited a larger redshift of the stretching mode of C=O moieties within the carboxylate group on adsorption of **1** compared with Cu-MOP-t (4 and 1 cm<sup>-1</sup>, respectively), indicating the presence of stronger catalyst-substrate binding interaction in Cu-MOP-e.

It has been reported that the oxidative depolymerization of the **1** occurs via the participation of •OOH radicals, generated from O<sub>2</sub>.<sup>31</sup> EPR spectra of the reaction solutions using different catalysts were measured using

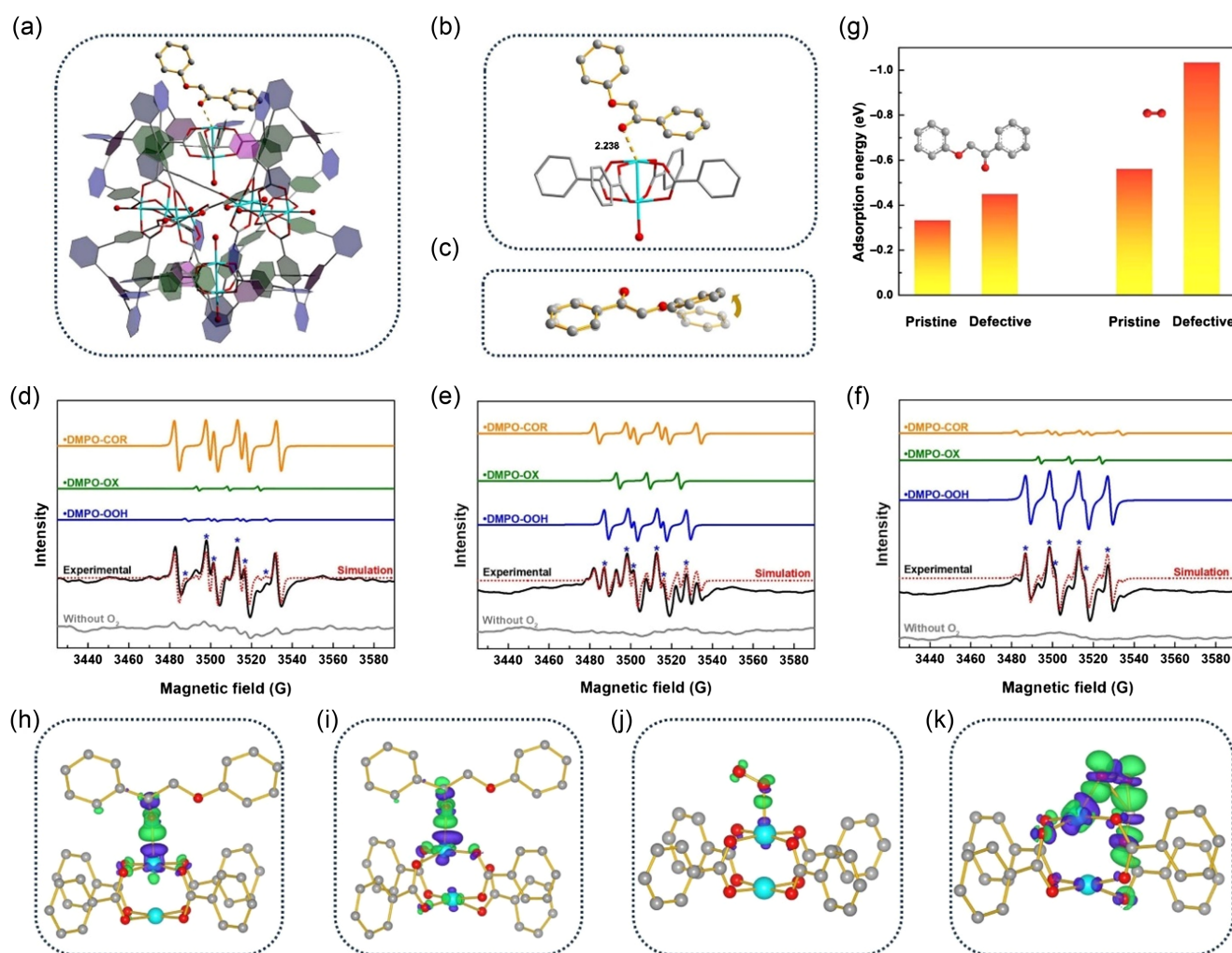


**Figure 4** | Mechanistic studies. (a, b) Structure of **1**-loaded Cu-MOP-t. (c) Change in torsion angle of **1** on binding to Cu-MOP-t. (d–f) EPR spectra of catalyst-free solution (d), Cu-MOP-t-containing solution (e) and Cu-MOP-e-containing solution (f). (g) Adsorption energy of **1** and O<sub>2</sub> on pristine and defective {Cu<sub>2</sub>}-paddlewheel. (h–k) Charge density diagrams of pristine {Cu<sub>2</sub>}-paddlewheel-**1** (h), defective {Cu<sub>2</sub>}-paddlewheel-**1** (i), pristine {Cu<sub>2</sub>}-paddlewheel-O<sub>2</sub> (j), defective {Cu<sub>2</sub>}-paddlewheel-O<sub>2</sub> (k). The green and blue regions represent electron donation and depletion, respectively, and the isosurface values are 0.002 e/Å<sup>3</sup> for (h) and (i) and 0.005 e/Å<sup>3</sup> for (j) and (k), respectively.

dimethyl pyridine *N*-oxide (DMPO) as a spin trap.<sup>43</sup> EPR signals were recorded after heating the samples at 90 °C for 5 min. Three types of radicals were identified with simulation (Figure 4d–f and Supporting Information Table S7) and were assigned as oxidized DMPO radical (•DMPO-OX,  $a_N = 15$  G), DMF radical (•DMPO-COR,  $a_N = 15.5$  G,  $a_H = 19$  G) and hydroperoxyl radical (•DMPO-OOH,  $a_N = 14.3$  G,  $a_H = 11.7$  G).<sup>44,45</sup> No •DMPO-OOH radical was detected in the absence of O<sub>2</sub>. All three radicals are involved equally using Cu-MOP-t as the catalyst, whereas the •DMPO-OOH radical was formed as the overwhelming species with Cu-MOP-e. Thus, Cu-MOP-e produced more •OOH radicals than Cu-MOP-t and catalyst-free systems (Supporting Information Figure S24) reflecting its higher activity for the cleavage of **1**.

DFT calculations were carried out to interrogate the interaction between the catalysts and reactants. As previously discussed, the Lewis acid sites originate from the breakage of Cu–O bonds. The pristine {Cu<sub>2</sub>}-paddlewheel and defective {Cu<sub>2</sub>}-paddlewheel represent Cu-MOP-t and Cu-MOP-e, respectively, in this analysis. The defective {Cu<sub>2</sub>}-paddlewheel exhibited higher adsorption energy of both **1** and O<sub>2</sub> (Figure 4g), the adsorption energy of O<sub>2</sub> on the defective {Cu<sub>2</sub>}-paddlewheel being twice as high as that of the pristine {Cu<sub>2</sub>}-paddlewheel. The charge density difference diagrams of pristine and defective {Cu<sub>2</sub>}-paddlewheel revealed that the latter was bound to **1** and O<sub>2</sub> (Figure 4h–k), thereby fostering a robust interaction with reactants that favored the reduction of the *Gibbs* free energy of the reaction.

Based on the preceding discussion, we propose a mechanism based upon the enhanced catalytic performance of Cu-MOP-e: During the reaction, the highly mesoporous structure enhances the accessibility of **1** to Cu-MOP-e, allowing **1** to be rapidly adsorbed onto the active centers. Additionally, the additional uncoordinated Cu(II) sites in Cu-MOP-e afford more active centers, enhancing interactions with **1** and O<sub>2</sub>. These stronger interactions facilitate the activation of **1** and the transformation of O<sub>2</sub> to •OOH radicals, thereby promoting the cleavage of **1** to phenol and benzoic acid.

## Conclusion

We show that Cu-MOP integrates hydrophobicity and hierarchical pores with open Cu(II) sites, and can be prepared via templated electrosynthesis to generate additional Lewis acid sites. Specifically, Cu-MOP-e exhibits an exceptional performance for the oxidative depolymerization of the lignin model compound **1**. The performance was significantly higher than Cu(II)-based MOFs owing to the promoted diffusion and mass transfer of the bulky substrate **1**, and the presence of open Cu(II) sites, along with open channels in Cu-MOP-e, resulting in stronger binding to the substrate. The intrinsic hydrophobicity of these Cu-MOPs not only drives the removal of Cu(II)-bound water to generate open Cu(II) sites but also affords excellent water stability and reusability for the recycled catalyst. This study promotes the design of new stable MOP-based catalysts by incorporating hierarchically porous structures and Lewis acid sites for heterogeneous catalysis in water.

## Supporting Information

Crystal data of **1**-loaded Cu-MOP are deposited at Cambridge Crystallographic Data Center (CCDC 2049508) and can be accessed free of charge from <https://www.ccdc.cam.ac.uk/structures>.

## Conflict of Interest

There is no conflict of interest to report.

## Funding Information

This work was supported by the Engineering and Physical Sciences Research Council (EPSRC), UK (grant nos. EP/I011870 and EP/K014706/2), the Royal Society, UK (grant no. IC170327), the National Natural Science Foundation of China (grant nos. 22273108, 21733011, and 21890761), the European Research Council (ERC) under the European Union's Horizon 2020 Research and Innovation Program, Brussels, Belgium (grant no. 742401,

NANOCHEM) and the Beijing Natural Science Foundation, China (grant no. 2222043).

## Acknowledgments

K.L. thanks the China Scholarship Council for their support. X.K. and A.S. research was supported by Royal Society Newton International Fellowships, UK. We acknowledge Diamond Light Source beamline staff and the UK Catalysis Hub Block Allocation Group (BAG) Programme Mode Application. The UK Catalysis Hub is kindly thanked for the resources and support provided via our membership of the UK Catalysis Hub Consortium.

## References

- Xu, W. Q.; Wu, Y.; Gu, W. L.; Du, D.; Lin, Y. H.; Zhu, C. Z. Atomic-Level Design of Metalloenzyme-Like Active Pockets in Metal-Organic Frameworks for Bioinspired Catalysis. *Chem. Soc. Rev.* **2024**, *53*, 137-162.
- Rousseau, B. J. G.; Soudackov, A. V.; Tuttle, R. R.; Reynolds, M. M.; Finke, R. G.; Hammes-Schiffer, S. Computational Insights into the Mechanism of Nitric Oxide Generation from S-Nitrosoglutathione Catalyzed by a Copper Metal-Organic Framework. *J. Am. Chem. Soc.* **2023**, *145*, 10285-10294.
- Yang, Y.; Kanchanakungwankul, S.; Bhaumik, S.; Ma, Q.; Ahn, S.; Truhlar, D. G.; Hupp, J. T. Bioinspired Cu(II) Defect Sites in ZIF-8 for Selective Methane Oxidation. *J. Am. Chem. Soc.* **2023**, *145*, 22019-22030.
- Peng, Y. G.; Tan, Q.; Huang, H. L.; Zhu, Q. G.; Kang, X. C.; Zhong, C. L.; Han, B. X. Customization of Functional MOFs by a Modular Design Strategy for Target Applications. *Chem. Synth.* **2022**, *2*, 15.
- Xu, S. J.; Chansai, S.; Stere, C.; Inceesungvorn, B.; Goguet, A.; Wangkawong, K.; Taylor, S. F. R.; Al-Janabi, N.; Hardacre, C.; Martin, P. A.; Fan, X. L. Sustaining Metal-Organic Frameworks for Water-Gas Shift Catalysis by Non-Thermal Plasma. *Nat. Catal.* **2019**, *2*, 142-148.
- Abednatanzi, S.; Najafi, M.; Derakhshandeh, P. G.; Van der Voort, P. Metal- and Covalent Organic Frameworks as Catalyst for Organic Transformation: Comparative Overview and Future Perspectives. *Coord. Chem. Rev.* **2022**, *451*, 214259.
- Gao, C. Y.; Tian, H. R.; Ai, J.; Li, L. J.; Dang, S.; Lan, Y. Q.; Sun, Z. M. A Microporous Cu-MOF with Optimized Open Metal Sites and Pore Spaces for High Gas Storage and Active Chemical Fixation of CO. *Chem. Commun.* **2016**, *52*, 11147-11150.
- Phan, A.; Doonan, C. J.; Uribe-Romo, F. J.; Knobler, C. B.; O'Keeffe, M.; Yaghi, O. M. Synthesis, Structure, and Carbon Dioxide Capture Properties of Zeolitic Imidazolate Frameworks. *Acc. Chem. Res.* **2010**, *43*, 58-67.
- He, T.; Kong, X. J.; Zhou, J.; Zhao, C.; Wang, K. C.; Wu, X. Q.; Lv, X. L.; Si, G. R.; Li, J. R.; Nie, Z. R. A Practice of Reticular Chemistry: Construction of a Robust Mesoporous Palladium Metal-Organic Framework via Metal Metathesis. *J. Am. Chem. Soc.* **2021**, *143*, 9901-9911.

10. Ji, Z.; Wang, H. Z.; Canossa, S.; Wuttke, S.; Yaghi, O. M. Pore Chemistry of Metal–Organic Frameworks. *Adv. Funct. Mater.* **2020**, *30*, 2000238.
11. Aguado, S.; Canivet, J.; Schuurman, Y.; Farrusseng, D. Tuning the Activity by Controlling the Wettability of MOF Eggshell Catalysts: A Quantitative Structure–Activity Study. *J. Catal.* **2011**, *284*, 207–214.
12. Dai, H.; Shen, Y. F.; Yang, T. M.; Lee, C. S.; Fu, D. L.; Agarwal, A.; Le, T. T.; Tsapatsis, M.; Palmer, J. C.; Weckhuysen, B. M.; Dauenhauer, P. J.; Zou, X. D.; Rimer, J. D. Finned Zeolite Catalysts. *Nat. Mater.* **2020**, *19*, 1074–1080.
13. Tranchemontagne, D. J. L.; Ni, Z.; O’Keeffe, M.; Yaghi, O. M. Reticular Chemistry of Metal–Organic Polyhedra. *Angew. Chem. Int. Ed.* **2008**, *47*, 5136–5147.
14. Carné-Sánchez, A.; Craig, G. A.; Larpent, P.; Hirose, T.; Higuchi, M.; Kitagawa, S.; Matsuda, K.; Urayama, K.; Furukawa, S. Self-Assembly of Metal–Organic Polyhedra into Supramolecular Polymers with Intrinsic Microporosity. *Nat. Commun.* **2018**, *9*, 2506.
15. Craig, G. A.; Larpent, P.; Kusaka, S.; Matsuda, R.; Kitagawa, S.; Furukawa, S. Switchable Gate-Opening Effect in Metal–Organic Polyhedra Assemblies Through Solution Processing. *Chem. Sci.* **2018**, *9*, 6463–6469.
16. Zhuang, S. P.; Huang, H. D.; Xiao, Y.; Zhang, Z. X.; Tang, J. H.; Gates, B. C.; Yang, D. Pair Sites on Al<sub>3</sub>O Nodes of the Metal–Organic Framework MIL-100: Cooperative Roles of Defect and Structural Vacancy Sites in Methanol Dehydration Catalysis. *J. Catal.* **2021**, *404*, 128–138.
17. Drake, T.; Ji, P. F.; Lin, W. B. Site Isolation in Metal–Organic Frameworks Enables Novel Transition Metal Catalysis. *Acc. Chem. Res.* **2018**, *51*, 2129–2138.
18. Fan, Z. Y.; Wang, J. J.; Wang, W. J.; Burger, S.; Wang, Z.; Wang, Y. M.; Wöll, C.; Cokoja, M.; Fischer, R. A. Defect Engineering of Copper Paddlewheel-Based Metal–Organic Frameworks of Type NOTT-100: Implementing Truncated Linkers and Its Effect on Catalytic Properties. *ACS Appl. Mater. Interfaces* **2020**, *12*, 37993–38002.
19. Wang, X. N.; Mao, N. N.; Bai, Y. L.; Zhuang, G. L.; Li, B. Two Self-Interpenetrating Copper(II)-Paddlewheel Metal–Organic Frameworks Constructed from Bifunctional Triazolate-Carboxylate Linkers. *Cryst. Growth Des.* **2018**, *18*, 6204–6210.
20. Chen, Y.; Wang, B.; Wang, X. Q.; Xie, L. H.; Li, J. P.; Xie, Y. B.; Li, J. R. A Copper(II)-Paddlewheel Metal–Organic Framework with Exceptional Hydrolytic Stability and Selective Adsorption and Detection Ability of Aniline in Water. *ACS Appl. Mater. Interfaces* **2017**, *9*, 27027–27035.
21. Argent, S. P.; da Silva, I.; Greenaway, A.; Savage, M.; Humby, J.; Davies, A. J.; Nowell, H.; Lewis, W.; Manuel, P.; Tang, C. C.; Blake, A. J.; George, M. W.; Markevich, A. V.; Besley, E.; Yang, S. H.; Champness, N. R.; Schröder, M. Porous Metal–Organic Polyhedra: Morphology, Porosity, and Guest Binding. *Inorg. Chem.* **2020**, *59*, 15646–15658.
22. Argent, S. P.; Greenaway, A.; Gimenez-Lopez, M. D.; Lewis, W.; Nowell, H.; Khlobystov, A. N.; Blake, A. J.; Champness, N. R.; Schröder, M. High-Nuclearity Metal–Organic Nanospheres: A Cd Ball. *J. Am. Chem. Soc.* **2012**, *134*, 55–58.
23. Fang, Z. L.; Bueken, B.; De Vos, D. E.; Fischer, R. A. Defect-Engineered Metal–Organic Frameworks. *Angew. Chem. Int. Ed.* **2015**, *54*, 7234–7254.
24. Sang, X. X.; Zhang, J. L.; Xiang, J. F.; Cui, J.; Zheng, L. R.; Zhang, J.; Wu, Z. H.; Li, Z. H.; Mo, G.; Xu, Y.; Song, J. L.; Liu, C. C.; Tan, X. N.; Luo, T.; Zhang, B. X.; Han, B. X. Ionic Liquid Accelerates the Crystallization of Zr-Based Metal–Organic Frameworks. *Nat. Commun.* **2017**, *8*, 175.
25. Greaves, T. L.; Kennedy, D. F.; Mudie, S. T.; Drummond, C. J. Diversity Observed in the Nanostructure of Protic Ionic Liquids. *J. Phys. Chem. B* **2010**, *114*, 10022–10031.
26. Karunakaran, C.; Balamurugan, M. *Spin Resonance Spectroscopy*; Elsevier Inc.: Amsterdam, **2018**; pp 169–197.
27. Ameloot, R.; Vermoortele, F.; Hofkens, J.; De Schryver, F. C.; De Vos, D. E.; Roefsaers, M. B. J. Three-Dimensional Visualization of Defects Formed During the Synthesis of Metal–Organic Frameworks: A Fluorescence Microscopy Study. *Angew. Chem. Int. Ed.* **2013**, *52*, 401–405.
28. Afanasenko, A. M.; Wu, X. Y.; De Santi, A.; Elgaher, W. A. M.; Kany, A. M.; Shafiei, R.; Schulze, M. S.; Schulz, T. F.; Hauptenthal, J.; Hirsch, A. K. H.; Barta, K. Clean Synthetic Strategies to Biologically Active Molecules from Lignin: A Green Path to Drug Discovery. *Angew. Chem. Int. Ed.* **2024**, *63*, e20230813.
29. Palumbo, C. T.; Gu, N. X.; Bleem, A. C.; Sullivan, K. P.; Katahira, R.; Stanley, L. M.; Kenny, J. K.; Ingraham, M. A.; Ramirez, K. J.; Haugen, S. J.; Amendola, C. R.; Stahl, S. S.; Beckham, G. T. Catalytic Carbon–Carbon Bond Cleavage in Lignin via Manganese-Zirconium-Mediated Autoxidation. *Nat. Commun.* **2024**, *15*, 862.
30. Zhou, H.; Jing, Y. X.; Wang, Y. Q. Activation/Cleavage of C–O/C–C Bonds During Biomass Conversion. *Acta Phys.-Chim. Sin.* **2022**, *38*, 2203016.
31. Yang, Y. Y.; Fan, H. L.; Song, J. L.; Meng, Q. L.; Zhou, H. C.; Wu, L. Q.; Yang, G. Y.; Han, B. X. Free Radical Reaction Promoted by Ionic Liquid: A Route for Metal-Free Oxidation Depolymerization of Lignin Model Compound and Lignin. *Chem. Commun.* **2015**, *51*, 4028–4031.
32. Ding, Y. M.; Guo, T. L.; Li, Z. W.; Zhang, B.; Kühn, F. E.; Liu, C.; Zhang, J.; Xu, D. Z.; Lei, M.; Zhang, T.; Li, C. Z. Transition-Metal-Free Synthesis of Functionalized Quinolines by Direct Conversion of β-O-4 Model Compounds. *Angew. Chem. Int. Ed.* **2022**, *61*, e202206284.
33. Zhang, B.; Guo, T. L.; Li, Z. W.; Kühn, F. E.; Lei, M.; Zhao, Z. B. K.; Xiao, J. L.; Zhang, J.; Xu, D. Z.; Zhang, T.; Li, C. Z. Transition-Metal-Free Synthesis of Pyrimidines from Lignin β-O-4 Segments via a One-Pot Multi-Component Reaction. *Nat. Commun.* **2022**, *13*, 3365.
34. Nguyen, J. D.; Matsuura, B. S.; Stephenson, C. R. J. A Photochemical Strategy for Lignin Degradation at Room Temperature. *J. Am. Chem. Soc.* **2014**, *136*, 1218–1221.
35. Yang, Y. Y.; Fan, H. L.; Meng, Q. L.; Zhang, Z. F.; Yang, G. Y.; Han, B. X. Ionic Liquid [OMIm][OAc] Directly Inducing Oxidation Cleavage of the β-O-4 Bond of Lignin Model Compounds. *Chem. Commun.* **2017**, *53*, 8850–8853.
36. Liu, C.; Wu, S. L.; Zhang, H. Y.; Xiao, R. Catalytic Oxidation of Lignin to Valuable Biomass-Based Platform Chemicals: A review. *Fuel Process Technol.* **2019**, *191*, 181–201.

37. Liu, Y. X.; Li, C. Z.; Miao, W.; Tang, W. J.; Xue, D.; Li, C. Q.; Zhang, B.; Xiao, J. L.; Wang, A. Q.; Zhang, T.; Wang, C. Mild Redox-Neutral Depolymerization of Lignin with a Binuclear Rh Complex in Water. *ACS Catal.* **2019**, *9*, 5583–5583.
38. Xia, S. X.; Nie, R. F.; Lu, X. Y.; Wang, L. N.; Chen, P.; Hou, Z. Y. Hydrogenolysis of Glycerol over  $\text{Cu}_{0.4}/\text{Zn}_{5.6}\text{Mg}_x\text{Al}_2\text{O}_{8.6}$  Catalysts: The Role of Basicity and Hydrogen Spillover. *J. Catal.* **2012**, *296*, 1–11.
39. Song, W. L.; Dong, Q. M.; Hong, L.; Tian, Z. Q.; Tang, L. N.; Hao, W. L.; Zhang, H. X. Activating Molecular Oxygen with Au/CeO<sub>2</sub> for the Conversion of Lignin Model Compounds and Organosolv Lignin. *RSC Adv.* **2019**, *9*, 31070–31077.
40. Wang, M.; Li, L. H.; Lu, J. M.; Li, H. J.; Zhang, X. C.; Liu, H. F.; Luo, N. C.; Wang, F. Acid Promoted C–C Bond Oxidative Cleavage of  $\beta$ -O-4 and  $\beta$ -1 Lignin Models to Esters over a Copper Catalyst. *Green Chem.* **2017**, *19*, 702–706.
41. Carter, J. H.; Han, X.; Moreau, F. Y.; da Silva, I.; Nevin, A.; Godfrey, H. G. W.; Tang, C. C.; Yang, S. H.; Schröder, M. Exceptional Adsorption and Binding of Sulfur Dioxide in a Robust Zirconium-Based Metal–Organic Framework. *J. Am. Chem. Soc.* **2018**, *140*, 15564–15567.
42. Takezawa, H.; Shitozawa, K.; Fujita, M. Enhanced Reactivity of Twisted Amides Inside a Molecular Cage. *Nat. Chem.* **2020**, *12*, 574–578.
43. Villamena, F. A.; Locigno, E. J.; Rockenbauer, A.; Hadad, C. M.; Zweier, J. L. Theoretical and Experimental Studies of the Spin Trapping of Inorganic Radicals by 5,5-dimethyl-1-pyrroline-oxide (DMPO): 1. Carbon Dioxide Radical Anion. *J. Phys. Chem. A* **2006**, *110*, 13253–13258.
44. Buettner, G. R. Spin Trapping: ESR Parameters of Spin Adducts. *Free Radical Biol. Med.* **1987**, *3*, 259–303.
45. Sinha, B. K. Enzymatic Activation of Hydrazine Derivatives. A Spin-Trapping Study. *J. Biol. Chem.* **1983**, *258*, 796–801.